Liquid metal–organic frameworks

Romain Gaillac[1,2], Pluton Pullumbi[2], Kevin A. Beyer[3], Karena W. Chapman[3], David A. Keen[4], Thomas D. Bennett[5]★ and François-Xavier Coudert[1]★

Metal–organic frameworks (MOFs) are a family of chemically diverse materials, with applications in a wide range of fields, covering engineering, physics, chemistry, biology and medicine. Until recently, research has focused almost entirely on crystalline structures, yet now a clear trend is emerging, shifting the emphasis onto disordered states, including 'defective by design' crystals, as well as amorphous phases such as glasses and gels. Here we introduce a strongly associated MOF liquid, obtained by melting a zeolitic imidazolate framework. We combine *in situ* variable temperature X-ray, *ex situ* neutron pair distribution function experiments, and first-principles molecular dynamics simulations to study the melting phenomenon and the nature of the liquid obtained. We demonstrate from structural, dynamical, and thermodynamical information that the chemical configuration, coordinative bonding, and porosity of the parent crystalline framework survive upon formation of the MOF liquid.

Crystalline metal–organic frameworks (MOFs) have been proposed for application in a variety of situations which take advantage of their highly ordered and nanoporous structures—for example, gas sorption and separation[1–3], catalysis[4] and ion transport[5]. Inherent defects[6], structural disorder[7] and near-ubiquitous flexibility[8] present significant challenges in the development of highly robust, selective systems from perfect crystals. However, they also present opportunities, in creating functional 'defective by design' materials[9,10].

Non-crystalline, or amorphous MOF systems are formed by avoidance of crystallization, or induced collapse of crystalline systems by pressure, temperature, or ball-milling[11]. In the case of the zeolitic imidazolate framework (ZIF) family[12,13], which adopt similar structures to inorganic zeolites and are formed from M^{n+} ($M^{n+} =$ for example, Li^+, B^+, Zn^{2+}) inorganic nodes connected by Im-based (Im = imidazolate, $C_3H_3N_2^-$) ligands, such amorphous systems resemble the continuous random network of amorphous SiO_2. Recently, the formation of a molten ZIF state from a crystalline phase was observed in an inert argon atmosphere. No mass loss was observed during the formation of the liquid, which upon cooling yielded a melt-quenched glass, possessing an extended Zn–Im–Zn coordination network[14]. Unlike reversible solid–liquid transitions in one- or two-dimensional coordination polymers which occur below 500 K (ref. 15), melting processes in ZIFs have been observed only at high temperatures, that is, those exceeding 700 K.

The novelty of the liquid and glass states means microscopic insight into the mechanism of melting, and the nature of the liquid produced are of great interest when considering the generality of the mechanism in the wider MOF family. However, thus far, the narrow temperature range and poorly understood kinetics-time stability of the fleeting liquid phase have precluded information on any liquid MOF state. Particularly salient and intriguing considerations pertaining to the liquid involve 'memory' of the crystalline framework conferred by remnant framework connectivity, coordinative framework dynamics and the proximity of structure to that of an ionic or a strongly associated liquid[16].

The ability to form hybrid 'porous liquids', analogous to that of the organic systems of the Cooper and James groups[17], would present a significant advance in the field, and help shift attention away from the solid state.

Motivated by the above questions and linking the MOF field to liquid, glass and polymer science, we studied the melting of ZIF-4 via experimental and computational means. The dynamic nature of the transition necessitated use of first-principles molecular dynamics (FPMD) calculations, which have previously been successfully used in ionic liquid and disordered carbonate systems[18,19]. Results were then combined with *in situ* variable temperature X-ray and *ex situ* neutron pair distribution function (PDF) experiments to yield a complete picture of the melting process, and, for the first time, an insight into the structure of a MOF liquid.

Structural characterization upon heating and melting

We first studied the evolution in structure of ZIF-4, which is composed of $Zn(Im)_4$ tetrahedra linked by Zn–N coordinative bonds (Fig. 1a,b), and forms a three-dimensional, crystalline network containing a maximum cavity diameter of 4.9 Å (Fig. 1c). It shares a topology with that of the mineral variscite, $CaGa_2O_4$, and a melting point of about 865 K has previously been identified, although no atomistic modelling of experimental data has to date been performed on any MOF liquid or glass.

A sample of ZIF-4 was prepared and evacuated according to previous literature procedures[20], and heated to 865 K in an argon tube furnace, before natural cooling to room temperature. The density has previously been shown to increase upon formation of a dense crystalline phase from ZIF-4 (1.24 g cm^{-3} to 1.582 g cm^{-3}) and to 1.625 g cm^{-3} for the glass[21,22]. Neutron and X-ray total scattering data were then collected using the GEM Diffractometer at the ISIS spallation source, and the Diamond Light Source, UK, respectively. Conversion to the PDFs was performed after data corrections (see Methods). Reverse Monte Carlo (RMC) modelling was subsequently performed, using as a starting model a previous Zn–Im–Zn continuous random network (CRN) configuration, arising from an

[1]Chimie ParisTech, PSL Research University, CNRS, Institut de Recherche de Chimie Paris, 75005 Paris, France. [2]Air Liquide, Centre de Recherche Paris Saclay, 78354 Jouy-en-Josas, France. [3]X-ray Science Division, Advanced Photon Source, Argonne National Laboratory, 9700 South Cass Avenue, Argonne, Illinois 60439, USA. [4]ISIS Facility, Rutherford Appleton Laboratory, Harwell Campus, Didcot, Oxon OX11 0QX, UK. [5]Department of Materials Science and Metallurgy, University of Cambridge, 27 Charles Babbage Road, Cambridge CB3 0FS, UK. *e-mail: tdb35@cam.ac.uk; fx.coudert@chimie-paristech.fr
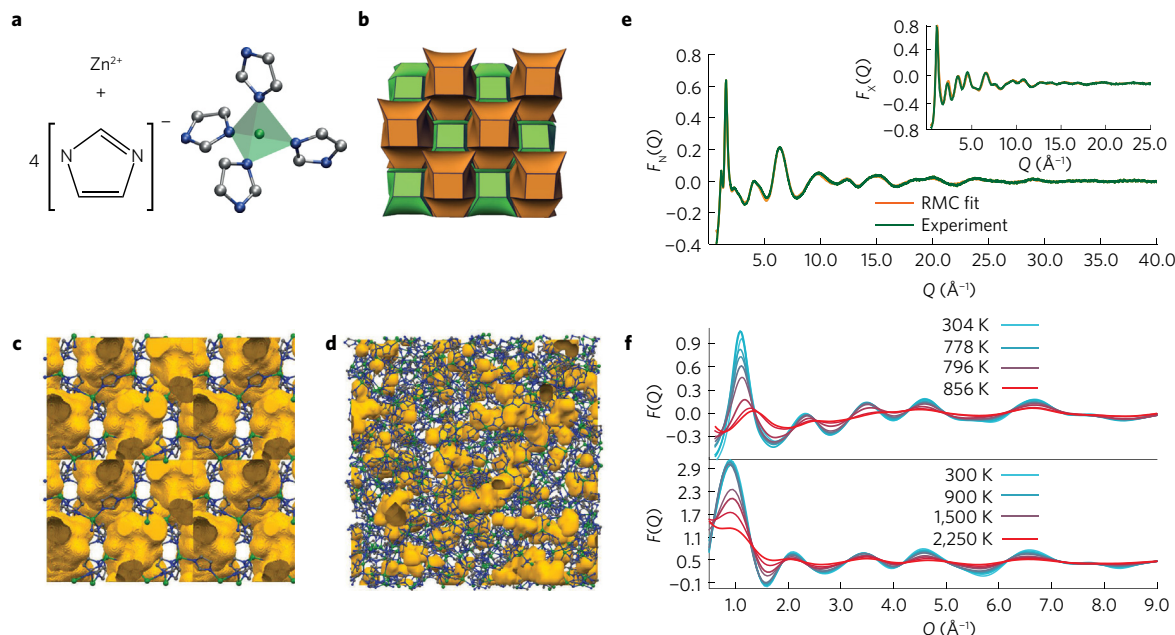
Figure 1 | Structure of the ZIF-4 crystal, glass, and structural evolution upon heating. a, The construction from metal ion and linker of Zn(Im)$_4$ tetrahedra, the basic building unit of ZIF-4 (Im, imidazolate; Zn, green; N, blue; C, grey). **b**, Representation of the cag topology adopted by ZIF-4, where each polyhedra corner corresponds to one Zn(Im)$_4$ tetrahedron. **c**, Crystalline structure of ZIF-4, with free volume represented in orange. **d**, Atomic configuration of the melt-quenched glass, gained from modelling synchrotron and neutron total scattering data. **e**, Experimental neutron structure factor $F(Q)$ data and the fit from the configuration shown in **d**. Inset: X-ray data and fit. **f**, Experimental glass (top) and computational ZIF-4 (bottom) X-ray structure factors upon heating.

amorphous, non-glass ZIF phase (that is, one which had not passed through the liquid state)[21]. No changes to the network topology were necessary, and the resultant configuration is shown in Fig. 1d. A good fit to the experimental structure factors was obtained (Fig. 1e), which reproduces all salient features. This model represents the first obtained using experimental data on a MOF glass.

Synchrotron X-ray diffraction data were then used to evaluate structural changes in the glass upon heating. Given the strong analogies of the structure of the melt-quenched ZIF glass to amorphous SiO$_2$, the density of the melt was approximated as 95% of that of the glass at T_m. Figure 1f shows the structure factor $F(Q)$ recorded from the glass at temperatures of 304, 778, 796 and 856 K on heating—while the corresponding total PDFs are plotted in Supplementary Fig. 1. The experimental structure factor for the glass at room temperature is largely similar to that previously reported[14], with no visible Bragg peaks. The PDF contains the expected peaks at approximately 1.3 Å, 2 Å, 3 Å, 4 Å and 6 Å, which correspond to C–C/C–N, Zn–N, Zn–C, Zn–N and Zn–Zn pair correlations, respectively.

Upon heating from 304 to 778 K, both the intensity and position of the first sharp diffraction peak (FSDP), centred at 1.1 Å^{-1}, remained approximately constant, as was the case with other visible features in the $F(Q)$. However, further heating to 856 K resulted in a more pronounced intensity reduction and a shift in the position of the FSDP to 1.3 Å^{-1}, along with a near-total disappearance of any features at higher Q values. This is in stark contrast to the case of liquid silica, where negligible changes in the FSDP upon melting are indicative of significant intermediate range order[23]. The changes in the $F(Q)$ result in a significantly decreased Zn–Zn correlation peak in the corresponding high-temperature PDFs, centred on 6 Å (Supplementary Fig. 1).

To probe the evolution of the ZIF structure upon heating and liquid formation from a microscopic point of view, we performed first-principles molecular dynamics simulation (FPMD) by running constant-temperature MD simulations at temperatures of 300, 600, 800, and up to 2,250 K. (Although the higher temperatures would not be physically relevant for the experimental system, they are made necessary by the relatively short times explored in FPMD, to gather statistics on relatively rare events and high thermodynamic barriers.) Because of the computational cost of FPMD, these simulations cannot be performed directly on the glass model—the unit cell of which is prohibitively large. Instead, we used the ZIF-4 crystalline phase as starting point, with the change in structure factor upon heating in good agreement with the trends observed experimentally (Fig. 1f). Similarly close agreement is also witnessed in the variable temperature total PDFs (see Supplementary Fig. 2).

Moreover, in addition to the total PDFs, we calculated from the MD trajectories the PDFs for specific atom–atom correlations, which provide greater understanding of the salient real-space structural movements. We plot in Fig. 2a–c the partial radial distribution functions $g_{ij}(r)$ for Zn–N, Zn–Im (where Im is the centre of mass of the imidazolate group) and Zn–Zn pairs. In addition to the overall thermal broadening of the peaks, there is a clear loss of long-range order at high temperature. At intermediate temperatures (around 1,000 K), the system has liquid-like disorder, with $g_{ij}(r)$ that do not go to zero after the first peak, although it retains some order at distances larger than 10 Å. To characterize further this state, we plot in Fig. 2d the generalized Lindemann ratio[24], computed from the width of the first peak in the Zn–N and Zn–Zn partial radial distribution functions. The usual criterion used to determine melting from the Lindemann ratio is between 10 and 15%, which indicates in our case a melting temperature between 1,000 and 1,500 K—and we note that the Zn–Zn ratio shows a clear disruption in slope at 1,200 K.

Thermodynamics of melting

Approaching the phenomenon from a thermodynamic standpoint, we plot in Fig. 2e the evolution of heat capacity C_V as a function of temperature. We see a clear jump in the heat capacity, indicative of a solid–liquid phase transition, from the value of the crystal phase ($C_V \approx 2.2\,\mathrm{J\,g^{-1}\,K^{-1}}$) to a higher value for the ZIF liquid ($C_V \approx 2.8\,\mathrm{J\,g^{-1}\,K^{-1}}$). Integration yields an estimate for the enthalpy of fusion of the ZIF of $\Delta H_\mathrm{fus} = 173\,\mathrm{J\,g^{-1}}$, which is in line with values
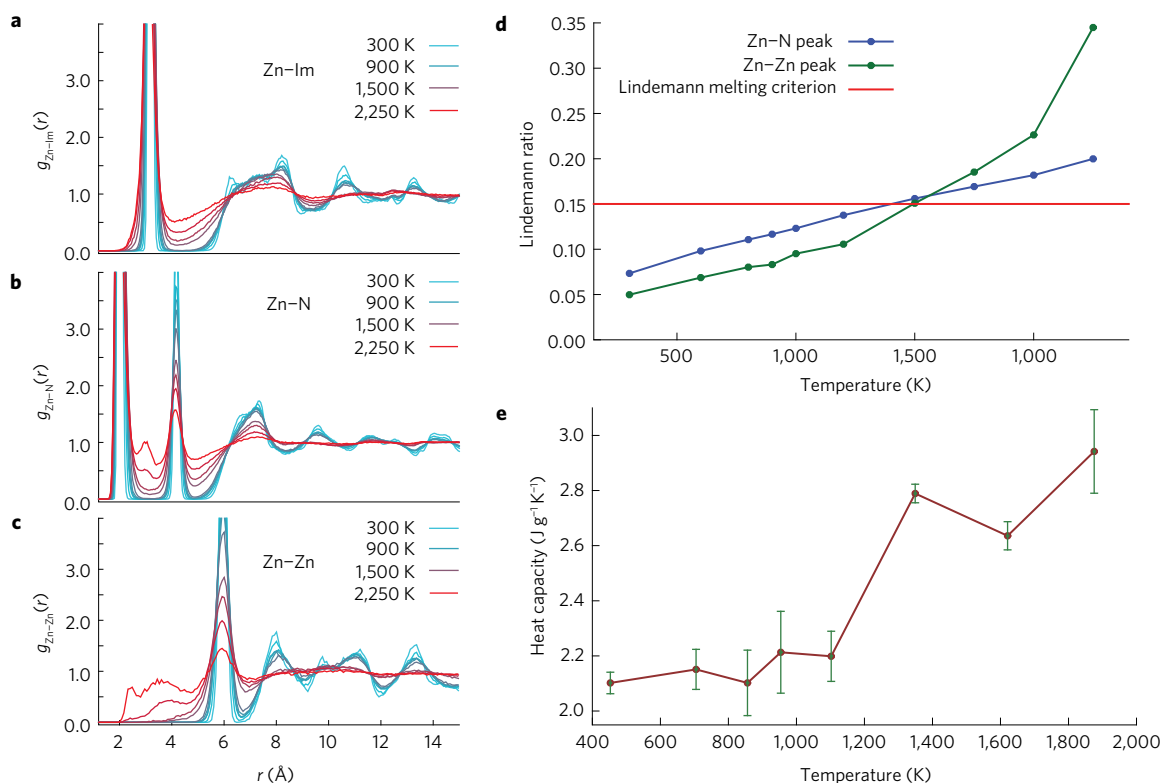
Figure 2 | Computational data from ZIF-4 melting: structure and thermodynamics. a–c, Evolution of the partial radial distribution function $g_{ij}(r)$ for Zn–Im distances (where Im is the centre of mass of the imidazolate group) (**a**), Zn–N distances (**b**) and Zn–Zn distances (**c**), at temperatures going from 300 K (light blue) to 2,250 K (red). **d**, Generalized Lindemann ratio Δ, quantifying the liquid nature of the system, as a function of temperature, calculated for Zn–Zn (green) and Zn–N (blue) interatomic distances. The red horizontal line represents the 'critical ratio' indicated in the literature at 10% or 15% (the value chosen here). **e**, Evolution of the heat capacity with temperature, with uncertainties calculated by block averaging over five different blocks of the trajectories.

for materials such as quartz ($\Delta H_{fus} = 146\,\mathrm{J\,g^{-1}}$) and cristobalite ($\Delta H_{fus} = 237\,\mathrm{J\,g^{-1}}$)[25].

Since the melting of this supramolecular network is dependent upon partial dissociation and reassociation of Zn–N coordination bonds, we used this distance as a reaction coordinate. From the Zn–N partial radial distribution function, $g_{Zn-N}(r)$, we calculated the potential of mean force (PMF) between the two atoms at all temperatures, through the relation $F(r) = -k_B T \ln g(r)$. From the resultant free energy profiles (Supplementary Fig. 3), we were then able to extract the temperature dependence of the activation free energy ($\Delta F^{\ddagger}$) needed to break the Zn–N bond. It can be seen in Supplementary Fig. 4 that $\Delta F^{\ddagger}$ follows a van 't Hoff law, $\Delta F^{\ddagger}(T) = \Delta H^{\ddagger} - T\Delta S^{\ddagger}$, with $\Delta H^{\ddagger} \approx 121\,\mathrm{kJ\,mol^{-1}}$ and $\Delta S^{\ddagger} \approx 34\,\mathrm{J\,mol^{-1}\,K^{-1}}$ in this temperature range.

The main contribution to the free energy barrier is thus energetic in nature, accompanied by a minor entropic stabilization. Moreover, the free energy barrier is still relatively high at the melting temperature, with $\Delta F^{\ddagger}(T = 1,000\,\mathrm{K}) = 87\,\mathrm{kJ\,mol^{-1}} = 10.5 k_B T$. Hence, as in conventional solids, melting occurs as a rare barrier-crossing event[26]. Finally, comparison of the potential of mean force for the Zn–Im coordinate with the PMF for Zn–N shows that breaking of the Zn–N bond is indeed an entirely suitable choice of reaction coordination for this activated process: as shown in Supplementary Table 1, the thermodynamic parameters are almost identical in both cases.

Microscopic mechanism

Turning to a molecular level visualization of the melting process, we depict in Fig. 3a,b the distribution of Zn cation coordination numbers as a function of temperature. The ideal fourfold

coordination is maintained at low temperatures up to 1,200 K, where more than 94% of the Zn ions are coordinated by four imidazolate groups. In this regime, the undercoordination of Zn^{2+} can be seen as a defect in the solid, and its concentration is found (as expected, Supplementary Fig. 5) to be proportional to $n_d \propto \exp(-\varepsilon/k_B T)$, where $\varepsilon \approx 56\,\mathrm{kJ\,mol^{-1}}$ is the energy required for defect formation. These 'undercoordinated' zinc ions can act as nucleation sites for melting. Going to higher temperature, the proportion of undercoordinated Zn^{2+} increases dramatically, for example, at 1,500 K with 59% in 4-fold coordination, 39% in 3-fold coordination, and 2% in 2-fold coordination. In contrast, we note that pentacoordination is almost nonexistent in our simulations.

Focusing on typical individual linker exchange events of zinc cations provides the mechanistic picture shown in Fig. 3d (snapshots from a FPMD simulation at 1,500 K); the melting process takes place over a few picoseconds through a sequence of well-defined steps. From an initial fourfold coordinated zinc, one imidazolate linker moves away and is then replaced by a neighbouring Im group with a dangling nitrogen lone pair. Inspired by Laage et al.'s statistical treatment of the molecular mechanism of reorientation in liquid water[27,28], we averaged over all events during a molecular dynamics trajectory to plot the average distance of the outgoing and incoming N atoms during an exchange—taking the reference time $t = 0$ when both nitrogen atoms are at equal distance from the zinc ion. This plot (Fig. 3c) shows that the event is concerted and that the exchange itself is rather fast, lasting less than 2 ps. This is very similar to what is seen for a switch between hydrogen bond partners in liquid water: both are strongly associated liquids forming a dynamic network with preferred tetrahedral association. The Zn–N bond or Zn–Im linkage breaking frequencies (see Supplementary Text,
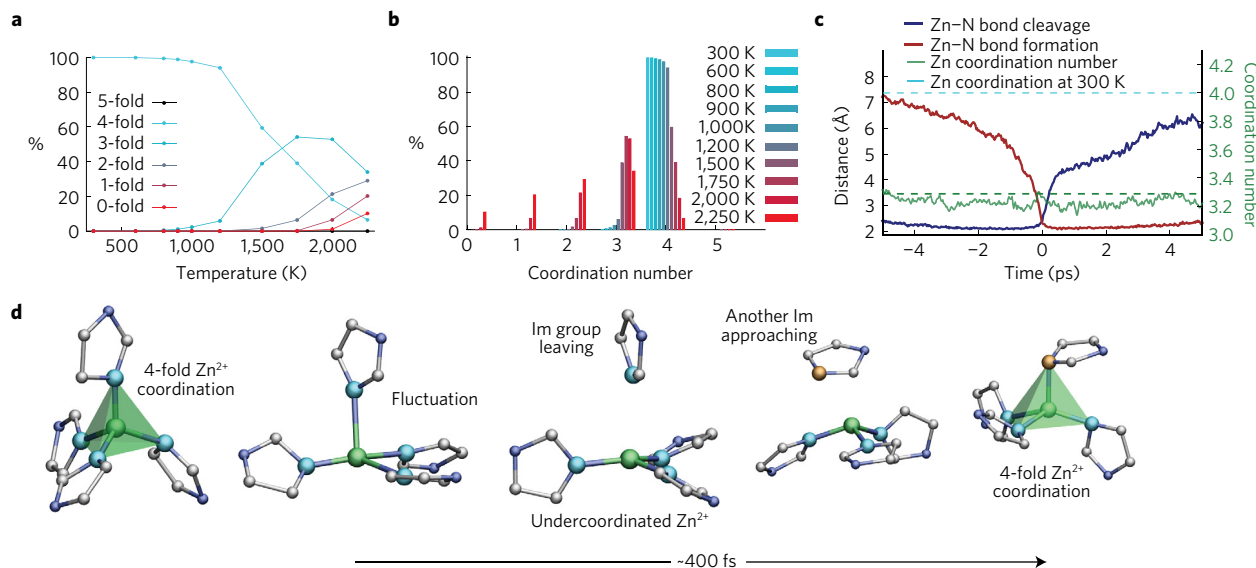
Figure 3 | Molecular mechanism of ZIF-4 melting. a, Distribution of zinc coordination numbers as a function of temperature, from 0-fold coordinated (red) to 4-fold (light blue). 5-fold coordination is indicated in black, but is close to the $y = 0$ axis. **b**, Temperature evolution for each degree of coordination of zinc cations. Temperatures range from 300 K (light blue) to 2,250 K (red). **c**, Behaviour during an exchange of a nitrogen atom by another nitrogen atom, in the first coordination sphere of a zinc cation, averaged over all such events (all exchanges on all zinc cations). The distance between the incoming nitrogen and the zinc is plotted in red, and that between the outgoing nitrogen and the zinc in blue. The green curve corresponds to the average coordination number of the zinc cation involved in the exchange. The flat dashed lines are the average coordination number over the whole simulation at 300 K (light blue) and 2,000 K (green). **d**, Visualization of a representative imidazolate exchange event. Zn, green; N (initially coordinated), light blue; N, blue; N (coordinated after exchange), orange; C, grey.

Supplementary Figs 6 and 7, and Supplementary Tables 2 and 3) demonstrate the Arrhenian behaviour of the system, reinforcing the idea that melting is driven by rare events disturbing the network.

Characterization of the liquid ZIF

To characterize the dynamics of the ZIF in the liquid phase, we calculated from our FPMD the translational diffusion of both zinc cations and imidazolate anions. The plots of mean square displacement over time, shown in Fig. 4a,b, clearly show diffusive behaviour at temperatures above 1,200 K—that is, in the liquid phase. The translational diffusion of zinc and imidazolate are clearly linked strongly, as the coefficients are very similar (see Supplementary Table 4) and both follow an Arrhenius law (see Supplementary Figs 8 and 9): for example, at 1,500 K we have $D_{Im} = 7.7 \ 10^{-10} \ m^2 \ s^{-1}$ and $D_{Zn} = 6.5 \ 10^{-10} \ m^2 \ s^{-1}$. This similarity in anion and cation diffusion is a rather common feature for ionic liquids. From these diffusion coefficients, we estimate the viscosity using the Stokes–Einstein relation ($\eta = kT/6\pi rD$): with a Zn^{2+} ionic radius of 88 pm, the viscosity at 1,500 K is 19 mPa s, and can be extrapolated by the Arrhenius law to 8,000 mPa s at 840 K, the experimental melting temperature. Analysis of linker rotations (see Supplementary Text) shows a regime of free rotation of the imidazolate linkers, at intermediate temperatures before melting.

Given the focus on porosity in MOFs, we investigated the nature of the liquid ZIF from a structural point of view. We performed statistical analysis of the instantaneous porosity along FPMD trajectories at all temperatures using a geometric criterion for the determination of porosity and a probe diameter of 2.4 Å, corresponding to the kinetic diameter of helium. The evolution of the pore volume distribution is depicted in Fig. 4c, from 300 K to higher temperatures. As expected for the solid phase ($T < 1,200$ K), a slight broadening of the distribution is observed, which corresponds to increased thermal motion. However, at higher temperatures, and particularly in the liquid phase, we see that the porosity is maintained overall, with only a slight deviation in average to lower pore volumes. This result, obtained in constant-volume simulations performed

at a density of 1.25 g cm^{-3} inferred from the experimentally available data, was confirmed by shorter constant-pressure simulations. Moreover, analysis of the accessible pore volume (that is, excluding nonconnected void pockets) shows in Supplementary Fig. 10 that a large fraction of the void space in the ZIF liquid is accessible porosity (going from 74% in crystalline ZIF-4 at 300 K to 95% in the liquid at 1,500 K). We thus conclude that, even at very high temperatures, the ZIF forms a hybrid 'porous liquid', quite different in nature from the organic systems recently reported[17], which are formed from cage molecules providing a well-defined pore space in solvents whose molecules are too bulky to enter the pores[29,30]. This finding is in agreement with the available experimental data on the free volume of ZIF glasses[31]. This porosity is found to be larger than that typical of imidazolium ionic liquids (whose ions are roughly of the same size as the imidazolate anion): those systems feature void space whose size distribution is typically negligible above 1 Å in radius[32,33].

To link the predicted liquid structure to experimental information, we performed RMC modelling on the X-ray total scattering data collected at 856 K (Fig. 1f). The atomistic configuration derived for the glass in Fig. 1d was used as a starting model, with a reduced density to reflect the changes upon melting. The final configuration is shown in Fig. 4d, along with the fit to the experimental X-ray structure factor (Supplementary Fig. 11). Whereas the internal surface of the glass at ambient temperature was calculated to be 4.8%, again using a standard probe diameter of 2.4 Å, that of the liquid at 856 K increased to 16.2%. Whilst transient in nature, linked voids appear irregularly distributed throughout the configuration.

Perspectives

In this work, we introduce the general term 'MOF liquid', for a liquid formed from the melting of a MOF, due to the retention of chemical configuration and coordinative bonding modes between the solid and liquid phases. Importantly, we show the retention of porosity in the liquid state, with a pore volume larger than in the glass state, making liquid ZIF-4 a rare example of an intrinsically porous liquid, enabling a compromise between the selectivity of
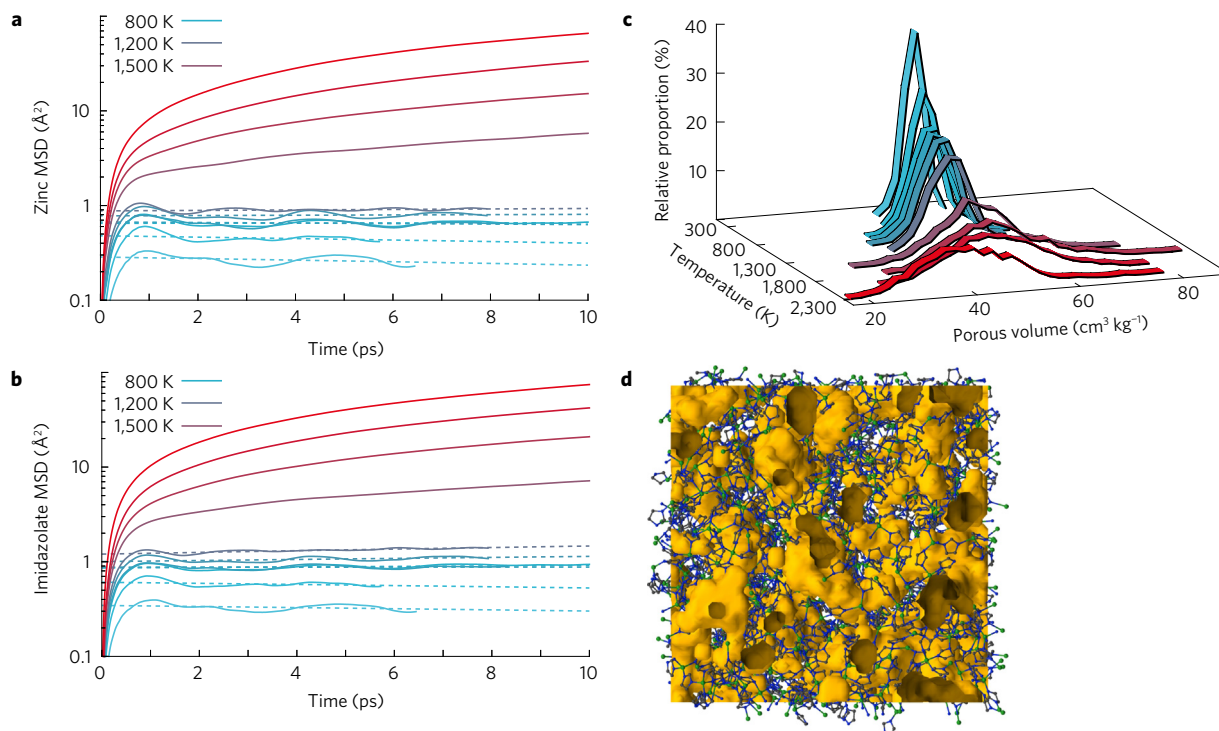
Figure 4 | Structure and dynamics in the ZIF liquid. a,b, Mean square displacement (MSD) as a function of time for zinc cations (**a**) and the centre of mass of the imidazolate linkers (**b**), plotted in logarithmic scale, for temperatures ranging from 300 K (light blue) to 2,250 K (red). Dashed curves represent fits of the MSD (excluding short times) for lower temperatures, showing the absence of diffusive behaviour. **c**, Temperature evolution of the distribution of the total pore volume, determined for a standard probe of radius 1.2 Å. The average pore volume takes the following values: 52 cm^3 kg^{-1} at 300 K, 49 cm^3 kg^{-1} at 2,000 K, and 41 cm^3 kg^{-1} at 2,250 K. **d**, Atomic configuration of the ZIF melt, gained from reverse Monte Carlo modelling of the total scattering data collected at 856 K. Free volume is represented in orange, Zn atoms in green, N in blue, and C in grey.

crystalline MOFs and diffusivity of amorphous membranes[34]. The demonstration and rationalization of melting in ZIF-4 provides a prototypical example in this new area, and a foundation on which further studies can be based, thus opening the way to the design or identification of other MOFs with accessible liquid or glass phases. The generality of the phenomenon depends upon a complex balance of melting temperature T_m and ligand decomposition temperature T_d. The latter is dependent on a multitude of factors, including atmosphere, heating rate and particle size, with faster heating rates of larger particles in inert atmospheres observed to prolong degradation temperatures from about 473 K to 773 K for ZIF-8 (refs 35,36). It is also, however, dependent upon chemistry, with species such as nitroimidazole undergoing early thermal decomposition due to C–NO$_2$ bond cleavage. This is consistent with the experimental observation that ZIFs containing NO$_2$-functionalized ligands decompose at about 573 K, compared with 773 K for ZIF-4 and ZIF-8 (ref. 37).

To probe the generic nature of the ZIF melting, we investigated the high-temperature behaviour of ZIF-8, which experimentally does not melt, through simulations. In these we do observe the melting of ZIF-8, but at higher temperature than for ZIF-4, as evidenced by the fourfold coordination of zinc that is retained up to 1,250 K (Supplementary Fig. 12). The calculated PMF (Supplementary Fig. 13) along the Zn–N coordinate for ZIF-8 give insight into its higher T_m: the activation free energy $\Delta F^\ddagger$ for zinc–imidazole bond breaking is significantly larger for ZIF-8 than for ZIF-4, due to a higher activation enthalpy $\Delta H^\ddagger$ (145 versus 127 kJ mol^{-1}, Supplementary Fig. 14). We thus see that the strength of ionic interaction between metal cation and organic anion plays a key role in determining T_m, with lower interaction strengths favouring melting.

In terms of extending this phenomenon to other families of MOFs, guidance may be given by the work of Horike *et al.* on phosphate-based coordination polymers[15]. Here, the interaction strength between a tetrahedral Zn^{2+} ion and one phosphate ligand was reduced due to additional interaction between the phosphate and imidazole. Whilst optical images of the crystal and glass states of ZIF-4 infer a high viscosity at T_m (ref. 22), a decrease in interaction strength would also result in a decrease in viscosity. As demonstrated in Cooper, James *et al.*[17], such liquid gas separation solutions offer major advantages over their solid porous counterparts due to the ease with which they can be applied in existing industrial plants. They also present an opportunity to shape MOFs on the macroscale, by using the liquid as a transient state *en route* to a glass, or recrystallized product. The glasses formed have already been shown to have unique mechanical and chemical properties when compared to existing organic, inorganic or metallic categories[14,38].

Chemically tunable porous MOF liquids with tailored properties reminiscent of crystalline structures will prove accessible through modification of inorganic centres and linker functionalization, length and shape—similar to those routinely used in the design and synthesis of MOF crystal structures. Such materials would be of interest for liquid phase separations, homogeneous catalysis and ion transport, alongside as an intermediary state in the formation of mechanically and thermally stable MOF glasses retaining porous characteristics.

Methods

Methods, including statements of data availability and any associated accession codes and references, are available in the online version of this paper.

References

1. Mason, J. A. *et al*. Methane storage in flexible metal-organic frameworks with intrinsic thermal management. *Nature* **527,** 357–361 (2015).
2. Rodenas, T. *et al*. Metal–organic framework nanosheets in polymer composite materials for gas separation. *Nat. Mater.* **14,** 48–55 (2014).
3. Yoon, J. W. *et al*. Selective nitrogen capture by porous hybrid materials containing accessible transition metal ion sites. *Nat. Mater.* **16,** 526–531 (2017).
4. Mondloch, J. E. *et al*. Destruction of chemical warfare agents using metal-organic frameworks. *Nat. Mater.* **14,** 512–516 (2015).
5. Horike, S., Umeyama, D. & Kitagawa, S. Ion conductivity and transport by porous coordination polymers and metal–organic frameworks. *Acc. Chem. Res.* **46,** 2376–2384 (2013).
6. Sholl, D. S. & Lively, R. P. Defects in metal–organic frameworks challenge or opportunity? *J. Phys. Chem. Lett.* **6,** 3437–3444 (2015).
7. Cairns, A. B. & Goodwin, A. L. Structural disorder in molecular framework materials. *Chem. Soc. Rev.* **42,** 4881–4893 (2013).
8. Schneemann, A. *et al*. Flexible metal-organic frameworks. *Chem. Soc. Rev.* **43,** 6062–6096 (2014).
9. Morris, R. E. & Čejka, J. Exploiting chemically selective weakness in solids as a route to new porous materials. *Nat. Chem.* **7,** 381–388 (2015).
10. Bennett, T. D., Cheetham, A. K., Fuchs, A. H. & Coudert, F.-X. Interplay between defects, disorder and flexibility in metal-organic frameworks. *Nat. Chem.* **9,** 11–16 (2017).
11. Bennett, T. D. & Cheetham, A. K. Amorphous metal–organic frameworks. *Acc. Chem. Res.* **47,** 1555–1562 (2014).
12. Park, K. S. *et al*. Exceptional chemical and thermal stability of zeolitic imidazolate frameworks. *Proc. Natl Acad. Sci. USA* **103,** 10186–10191 (2006).
13. Tian, Y.-Q. *et al*. Design and generation of extended zeolitic metal-organic frameworks (ZMOFs): synthesis and crystal structures of zinc(II) imidazolate polymers with zeolitic topologies. *Chem. Eur. J.* **13,** 4146–4154 (2007).
14. Bennett, T. D. *et al*. Hybrid glasses from strong and fragile metal-organic framework liquids. *Nat. Commun.* **6,** 8079 (2015).
15. Umeyama, D., Horike, S., Inukai, M., Itakura, T. & Kitagawa, S. Reversible solid-to-liquid phase transition of coordination polymer crystals. *J. Am. Chem. Soc.* **137,** 864–870 (2015).
16. MacFarlane, D. R. *et al*. Ionic liquids and their solid-state analogues as materials for energy generation and storage. *Nat. Rev. Mater.* **1,** 15005 (2016).
17. Giri, N. *et al*. Liquids with permanent porosity. *Nature* **527,** 216–220 (2015).
18. Kohara, S. *et al*. Atomic and electronic structures of an extremely fragile liquid. *Nat. Commun.* **5,** 5892 (2014).
19. Corradini, D., Coudert, F.-X. & Vuilleumier, R. Carbon dioxide transport in molten calcium carbonate occurs through an oxo-Grotthuss mechanism via a pyrocarbonate anion. *Nat. Chem.* **8,** 454–460 (2016).
20. Wharmby, M. T. *et al*. Extreme flexibility in a zeolitic imidazolate framework: porous to dense phase transition in desolvated ZIF-4. *Angew. Chem. Int. Ed.* **54,** 6447–6451 (2015).
21. Bennett, T. D. *et al*. Structure and properties of an amorphous metal–organic framework. *Phys. Rev. Lett.* **104,** 115503 (2010).
22. Bennett, T. D. *et al*. Melt-quenched glasses of metal–organic frameworks. *J. Am. Chem. Soc.* **138,** 3484–3492 (2016).
23. Mei, Q., Benmore, C. J. & Weber, J. K. R. Structure of liquid SiO_2: a measurement by high-energy X-ray diffraction. *Phys. Rev. Lett.* **98,** 057802 (2007).
24. Chakravarty, C., Debenedetti, P. G. & Stillinger, F. H. Lindemann measures for the solid-liquid phase transition. *J. Chem. Phys.* **126,** 204508 (2007).
25. Kelly, K. Heats of Fusion of Inorganic Compounds. *US Bur. Mines Bull.* **393,** 152 (1936).
26. Samanta, A., Tuckerman, M. E., Yu, T.-Q. & E, W. Microscopic mechanisms of equilibrium melting of a solid. *Science* **346,** 729–732 (2014).
27. Laage, D. & Hynes, J. T. A molecular jump mechanism of water reorientation. *Science* **311,** 832–835 (2006).
28. Laage, D. & Hynes, J. T. On the molecular mechanism of water reorientation. *J. Phys. Chem. B* **112,** 14230–14242 (2008).
29. O'Reilly, N., Giri, N. & James, S. L. Porous liquids. *Chem. Eur. J.* **13,** 3020–3025 (2007).
30. Hasell, T. & Cooper, A. I. Porous organic cages: soluble, modular and molecular pores. *Nat. Rev. Mater.* **1,** 16053 (2016).
31. Thornton, A. W. *et al*. Porosity in metal-organic framework glasses. *Chem. Commun.* **52,** 3750–3753 (2016).
32. Forero-Martinez, N. C., Cortes-Huerto, R. & Ballone, P. The glass transition and the distribution of voids in room-temperature ionic liquids: a molecular dynamics study. *J. Chem. Phys.* **136,** 204510 (2012).
33. Deschamps, J., Costa Gomes, M. F. & Pádua, A. A. H. Molecular simulation study of interactions of carbon dioxide and water with ionic liquids. *ChemPhysChem* **5,** 1049–1052 (2004).
34. Freeman, B. D. Basis of permeability/selectivity tradeoff relations in polymeric gas separation membranes. *Macromolecules* **32,** 375–380 (1999).
35. Pimentel, B. R., Parulkar, A., Zhou, E.-k., Brunelli, N. A. & Lively, R. P. Zeolitic imidazolate frameworks: next-generation materials for energy-efficient gas separations. *ChemSusChem* **7,** 3202–3240 (2014).
36. James, J. B. & Lin, Y. S. Kinetics of ZIF-8 thermal decomposition in inert, oxidizing, and reducing environments. *J. Phys. Chem. C* **120,** 14015–14026 (2016).
37. Bennett, T. D., Saines, P. J., Keen, D. A., Tan, J.-C. & Cheetham, A. K. Ball-milling-induced amorphization of zeolitic imidazolate frameworks (ZIFs) for the irreversible trapping of iodine. *Chem. Eur. J.* **19,** 7049–7055 (2013).
38. Nagarkar, S. S. *et al*. Enhanced and optically switchable proton conductivity in a melting coordination polymer crystal. *Angew. Chem. Int. Ed.* **56,** 4976–4981 (2017).

Author contributions

T.D.B. and F.-X.C. designed the project. T.D.B. and D.A.K. performed the total scattering experiments, D.A.K. performed all RMC profile experiments and led the data correction. K.W.C. and K.A.B. contributed to the variable temperature total scattering experiments at the Advanced Photon Source. R.G. performed the molecular simulations, which R.G. and F.-X.C. analysed. All authors participated in discussing the data. R.G., T.D.B. and F.-X.C. wrote the manuscript with input from all authors.

Additional information

Supplementary information is available in the online version of the paper. Reprints and permissions information is available online at www.nature.com/reprints. Publisher's note: Springer Nature remains neutral with regard to jurisdictional claims in published maps and institutional affiliations. Correspondence and requests for materials should be addressed to T.D.B. or F.-X.C.

Competing financial interests

The authors declare no competing financial interests.

Methods

Neutron total scattering. A sample of deuterated ZIF-4 was prepared by directly substituting $C_3D_4N_2$ for $C_3H_4N_2$ in the synthetic methodology previously reported for ZIF-4 (ref. 20), and melt-quenched according to published procedures[14]. Data were measured at room temperature using the GEM diffractometer at ISIS[39] on a sample which filled a 6-mm-diameter thin-walled cylindrical vanadium can to 36 mm. Suitable background subtraction and corrections were performed using measurements from an empty vanadium can, empty instrument, 8 mm V-5.14% Nb rod, and the Gudrun software[39].

X-ray total scattering (room temperature). Data were collected at the I15-1 beamline at the Diamond Light Source, UK ($\lambda = 0.158345$ Å, 78.3 keV). A small amount of the sample used in the neutron total scattering experiment was loaded into a glass capillary of 0.76 mm diameter. Data on the sample, empty instrument and capillary were collected in the region of $\sim 0.4 < Q < \sim 26$ Å^{-1}. Background, multiple scattering, container scattering, Compton scattering and absorption corrections were performed using the GudrunX program[40,41].

X-ray total scattering (variable temperature). Measurements were performed on a sample of melt-quenched ZIF-4 glass produced in an identical manner to those used for the X-ray room temperature measurements. Data were collected at the Advanced Photon Source, USA on the 11-ID-B beamline ($\lambda = 0.143$ Å, 86.7 keV), in the range $0.6 < Q < \sim 24$ Å^{-1}. A finely ground sample of the glass was loaded into a 1-mm-diameter silica capillary, along with glass wool to hold it in place during the melting process. Data were collected under flowing argon gas at room temperature, and then upon heating from 298 K in about 100 K steps to 778 K. Subsequent measurements were performed every 6 K. Data were corrected in the same manner as the room-temperature X-ray measurements.

Reverse Monte Carlo modelling. To produce the structural configuration of the melt-quenched glass, the RMCProfile software[42] was used to refine an atomistic starting model for an amorphous, non-melt-quenched ZIF described previously[21], against the neutron and X-ray $F(Q)$ and neutron PDF room-temperature data. The resultant configuration was then used as a starting input model for an RMCProfile refinement of the structure of the liquid, using the X-ray total scattering data collected at 856 K. The density of the model was adjusted to match that determined experimentally for the glass and liquid phases (the densities used are summarized in Supplementary Table 5).

First-principles molecular dynamics. The behaviour of zeolitic imidazolate frameworks as a function of temperature was studied by means of density functional theory (DFT)-based molecular dynamics (MD) simulations, using the Quickstep module[43] of the CP2K software package[44]. We used the hybrid Gaussian and plane-wave method GPW as implemented in CP2K. The simulations were performed in the constant-volume (N, V, T) ensemble with fixed size and shape of the unit cell. A timestep of 0.5 fs was used in the MD runs and the temperature was controlled by velocity rescaling[45]. MD simulations consisted of an equilibration period of 5 ps and production period between 60 ps and 220 ps, depending on the temperature, to study the dynamics of the liquid.

The exchange–correlation energy was evaluated in the Perdew–Burke–Ernzerhof (PBE) approximation[46], and the dispersion interactions were treated at the DFT-D3 level[47]. The Quickstep module uses a multi-grid system to map the basis functions onto. We kept the default number of four different grids but chose a relatively high plane-wave cut-off for the electronic density to be 600 Ry, as already used in ref. 48, and a relative cut-off (keyword REL_CUTOFF in CP2K) of 40 Ry for high accuracy. Valence electrons were described by double-zeta valence polarized basis sets and norm-conserving Goedecker–Teter–Hutter[49] pseudopotentials, all adapted for PBE (DZVP-GTH-PBE) for H, C and N or optimized for solids (DZVP-MOLOPT-SR-GTH) in the case of Zn. Representative input files for the molecular dynamics simulations are available as supporting information, and online in our data repository at https://github.com/fxcoudert/citable-data.

The unit cell studied for ZIF-4 (space group *Pbca*) is the orthorhombic primitive unit cell, which contains 272 atoms, with cell parameters $a = 15.423$ Å, $b = 15.404$ Å, $c = 18.438$ Å, and $\alpha = \beta = \gamma = 90°$. These unit cell parameters were the result of a full geometry optimization (atomic and unit cell parameters) of the ZIF-4 crystal at 0 K. The density obtained is 1.25 g cm^{-3}, in good agreement with the crystallographic density of 1.22 g cm^{-3} at room temperature, and all simulations were performed with this density. To test the validity of the constant-volume approach (dictated by reasons of computation cost), we ran shorter constant-pressure (N, P, T) simulations at 300 K and 1,500 K. These simulations both yielded an average density of 1.22 g cm^{-3} (with instantaneous fluctuations of ± 0.09 g cm^{-3}), showing that the variations of density upon heating and melting are minimal. Finally, constant-volume FPMD simulations at 300 K and 1,500 K were performed at a density of 1.6 g cm^{-3}, and their structure factors are compared to those obtained at 1.25 g cm^{-3} in Supplementary Fig. 16.

Trajectory analysis. The Lindemann ratio Δ is computed from the width of the first peaks in the different partial radial distribution functions as a measure of the fluctuation of atomic positions and interparticular distances:

$$\Delta = \frac{\text{FWHM}}{d_0} \tag{1}$$

where FWHM is the full-width at half-maximum of the first partial radial distribution function peak (estimated by a Gaussian fit) and d_0 corresponds to the mean interatomic distance (calculated as the maximum of the first peak), that is, $d_0 = 5.95$ Å for Zn–Zn and $d_0 = 2.0$ Å for Zn–N.

The coordination number for nitrogen atoms around the zinc cation is computed by taking a cut-off radius of 2.5 Å, a value chosen from the Zn–N partial radial distribution function at room temperature. We checked that the precise value used does not influence the outcome of the calculations, nor does the choice of a discontinuous criterion (versus the use of a damping function near the cut-off value).

From the MD simulations, we can extract the internal energy $U(T)$ as the average of the total energy of the system. From these values we can then calculate the heat capacities $C_V(T)$ by finite differences:

$$C_v\left(\frac{T_1 + T_2}{2}\right) = \frac{U(T_2) - U(T_1)}{T_2 - T_1} \tag{2}$$

where T_1 and T_2 are two successive temperatures in our series of simulations. Uncertainties were calculated by block averaging over five different blocks of the trajectories. Furthermore, we can estimate the enthalpy of fusion by writing the energy difference in heating the system from $T_1 = 1,000$ K to $T_2 = 1,500$ K:

$$\Delta U = C_V(T_1) \times (T_2 - T_1) + \Delta H_{\text{fus}} \tag{3}$$

To compute the total porous volume, we used the freely available software Zeo++ (refs 50–52). It uses a geometric decomposition of space to compute the accessible and non-accessible volume to a sphere of a given radius. We have taken a value of 1.2 Å simulating the porous volume as seen by a helium molecule, calculating the distribution of instantaneous total pore space (sum of the accessible and the non-accessible volume) along the MD trajectories at each temperature. We also studied the evolution of the pore volume distribution as a function of probe radius at 1,500 K, as plotted in Supplementary Fig. 15.

Data availability. Experimental and computational data supporting the findings of this work are available from the public GitHub online repository at https://github.com/fxcoudert/citable-data.

References

39. Keen, D. A. A comparison of various commonly used correlation functions for describing total scattering. *J. Appl. Cryst.* **34,** 172–177 (2001).
40. Soper, A. K. *GudrunN and GudrunX: Programs for Correcting Raw Neutron and X-ray Diffraction Data to Differential Scattering Cross Section* Tech. Rep. RAL-TR-2011-013 (Rutherford Appleton Laboratory, 2011).
41. Soper, A. K. & Barney, E. R. Extracting the pair distribution function from white-beam X-ray total scattering data. *J. Appl. Cryst.* **44,** 714–726 (2011).
42. Tucker, M. G., Keen, D. A., Dove, M. T., Goodwin, A. L. & Hui, Q. RMCProfile: reverse Monte Carlo for polycrystalline materials. *J. Phys. Condens. Matter* **19,** 335218 (2007).
43. VandeVondele, J. *et al*. Quickstep: fast and accurate density functional calculations using a mixed Gaussian and plane waves approach. *Comput. Phys. Commun.* **167,** 103–128 (2005).
44. CP2K 4.1 (CP2K, 2016); http://www.cp2k.org
45. Bussi, G., Donadio, D. & Parrinello, M. Canonical sampling through velocity rescaling. *J. Chem. Phys.* **126,** 014101 (2007).
46. Perdew, J. P., Burke, K. & Ernzerhof, M. Generalized gradient approximation made simple. *Phys. Rev. Lett.* **77,** 3865–3868 (1996).
47. Grimme, S., Antony, J., Ehrlich, S. & Krieg, H. A consistent and accurate ab initio parametrization of density functional dispersion correction (DFT-D) for the 94 elements H-Pu. *J. Chem. Phys.* **132,** 154104 (2010).
48. Haigis, V., Coudert, F.-X., Vuilleumier, R. & Boutin, A. Investigation of structure and dynamics of the hydrated metal-organic framework MIL-53(Cr) using first-principles molecular dynamics. *Phys. Chem. Chem. Phys.* **15,** 19049–19056 (2013).
49. Goedecker, S., Teter, M. & Hutter, J. Separable dual-space Gaussian pseudopotentials. *Phys. Rev. B* **54,** 1703–1710 (1996).
50. Pinheiro, M. *et al*. Characterization and comparison of pore landscapes in crystalline porous materials. *J. Mol. Graph. Model.* **44,** 208–219 (2013).
51. Martin, R. L., Smit, B. & Haranczyk, M. Addressing challenges of identifying geometrically diverse sets of crystalline porous materials. *J. Chem. Inf. Model.* **52,** 308–318 (2012).
52. Willems, T. F., Rycroft, C. H., Kazi, M., Meza, J. C. & Haranczyk, M. Algorithms and tools for high-throughput geometry-based analysis of crystalline porous materials. *Micro. Meso. Mater.* **149,** 134–141 (2012).